Soft Matter

PAPER

View Article Online
View Journal | View Issue

Cite this: *Soft Matter*, 2023, **19**, 4964

3D printable adhesive elastomers with dynamic covalent bond rearrangement†

Shiwanka V. Wanasinghe,‡[a] Brent Johnson,‡[b] Rebekah Revadelo,[b] Grant Eifert,[b] Allyson Cox,[c] Joseph Beckett,[e] Timothy Osborn,[c] Carl Thrasher,*[d] Robert Lowe*[b] and Dominik Konkolewicz*[a]

Received 24th March 2023,
Accepted 12th June 2023

DOI: 10.1039/d3sm00394a

rsc.li/soft-matter-journal

Repairable adhesive elastomers are emerging materials employed in compelling applications such as soft robotics, biosensing, tissue regeneration, and wearable electronics. Facilitating adhesion requires strong interactions, while self-healing requires bond dynamicity. This contrast in desired bond characteristics presents a challenge in the design of healable adhesive elastomers. Furthermore, 3D printability of this novel class of materials has received limited attention, restricting the potential design space of as-built geometries. Here, we report a series of 3D-printable elastomeric materials with self-healing ability and adhesive properties. Repairability is obtained using Thiol–Michael dynamic crosslinkers incorporated into the polymer backbone, while adhesion is facilitated with acrylate monomers. Elastomeric materials with excellent elongation up to 2000%, self-healing stress recovery >95%, and strong adhesion with metallic and polymeric surfaces are demonstrated. Complex functional structures are successfully 3D printed using a commercial digital light processing (DLP) printer. Shape-selective lifting of low surface energy poly(tetrafluoroethylene) objects is achieved using soft robotic actuators with interchangeable 3D-printed adhesive end effectors, wherein tailored contour matching leads to increased adhesion and successful lifting capacity. The demonstrated utility of these adhesive elastomers provides unique capabilities to easily program soft robot functionality.

1. Introduction

Adhesion is the interaction between two surfaces through chemical or physical bonding.[1] The focus on adhesive materials has increased due to their widespread use in biomedical, aerospace, construction, packaging, and automotive applications.[2–6] In recent decades, polymer adhesives have enabled cost-effective material systems with excellent mechanical and surface properties.[7–10] As such, a vast library of adhesive materials has been reported in the literature.[1,11–13]

Adhesion mechanisms can often be considered as a function of both molecular and mechanical coupling.[1] Molecular coupling is the adhesion between two surfaces in close proximity through intermolecular forces such as dipole–dipole interactions, van der Waals forces, ionic interactions, metallic bonding, or covalent bonding.[1] Mechanical coupling, a function of the contact area, is the macroscopic interlocking of two surfaces using an adhesive material sandwiched between the surfaces.[1] This coupling is maximized when the adhesive material occupies irregularities, such as holes and peaks, on the interfacial surfaces.[14] The mechanisms of polymer adhesion are dependent on surface characteristics, and several factors should be considered when designing an adhesive polymer. Applications that need both cohesive and adhesive forces, such as glue, should maintain a balance between these two forces to avoid high affinity towards one of the surfaces.[10] In addition, the moduli of the adhesive and substrate should be optimized to yield a tough material system when adhered. In general, low-modulus adhesives are optimal for soft substrates, while high-modulus adhesives are optimal for hard substrates.[9] Ductility is another important parameter for optimizing adhesion, since low ductility can promote crack propagation.[4,5] In contrast, highly ductile materials use plastic deformation to disperse mechanical energy and increase toughness.[5] However, permanent damage from plastic deformation can reduce cohesive strength and lead to internal shear-driven material failure, especially during cyclic loading.

[a] *Department of Chemistry and Biochemistry, Miami University, Oxford, OH 45056, USA. E-mail: d.konkolewicz@miamioh.edu*
[b] *Department of Mechanical and Aerospace Engineering, University of Dayton, Dayton, OH 45469, USA. E-mail: rlowe1@udayton.edu*
[c] *Additive Manufacturing Technology Development Group, University of Dayton Research Institute, Dayton, OH 45469, USA*
[d] *Department of Materials Science and Engineering, Massachusetts Institute of Technology, Cambridge, MA 02142, USA. E-mail: cthrash@mit.edu*
[e] *Department of Mechanical Engineering, University of Michigan, Ann Arbor, MI 48109, USA*

† Electronic supplementary information (ESI) available. See DOI: https://doi.org/10.1039/d3sm00394a

‡ Contributed equally.

Self-healing elastomers with embedded damage repair are a novel class of materials that offer the potential for continuous, uninterrupted soft device operation.[15] One method for imparting self-healing characteristics into polymers is by incorporating dynamic bonds.[16] Developing polymers with both self-healing and adhesive properties is desirable but challenging, since the contrasting properties of bond dynamicity for self-healing and strong interactions for adhesion are required.[17] Although several self-healing elastomer adhesives have been reported,[2,6,13,17–22] the 3D printability of repairable adhesives has received limited attention.

3D printing is useful for producing custom structures with complex form factors. Several common 3D printing techniques for polymers include stereolithography, selective laser sintering, photo-curable inkjet printing, fused filament fabrication, and direct ink writing.[23] However, most of these techniques are limited by slow print speeds, poor scalability, and/or low resolution.[24] In contrast, digital light processing (DLP) 3D printing achieves high speed, scale, and resolution by utilizing patterned projected light to cure full layers of resin simultaneously.[25] This makes DLP 3D printing ideal for rapid prototyping or manufacturing high-complexity objects such as soft robots.[26]

Soft robotics is a field concerning adaptable and lightweight robots made with compliant materials.[27,28] Soft robots are increasingly being used in textiles, biological applications, and electronics applications.[3,27,29] Additionally, self-healing functionality is being included in soft robotic systems as a mechanism for embedded damage repair.[24,30] While DLP has been used to 3D print materials for soft robotics, balancing mechanical properties, printability, and responsive functionality (*e.g.*, self-healing, adhesion) remains a challenging task.

In this study, we designed a series of DLP-printable adhesive materials with self-healing ability. Self-healing was obtained using Thiol–Michael dynamic exchange (Fig. 1(b)), which was incorporated into the polymer through a diacrylate crosslinker. 2-Hydroxyethyl acrylate (HEA) and butyl acrylate (BA) were used as the polymer backbone, and Thiol–Michael-based sulfone diacrylate (TMSDA) was used as the dynamic Thiol–Michael crosslinker (Fig. 1(b)). BA was used to improve material tackiness, while 2,2′-(ethylenedioxy)diethanethiol (EDDT) was added to increase compliance and add extra thioether components into the material system.[24] Variations in composition were explored to show tunability in mechanical and adhesive properties. 3D printing of complex structures, including pneumatic actuators, with high fidelity was successfully demonstrated. Exploiting this 3D printability, functionality was added to an existing soft robotic actuator by adhering 3D-printed end effectors with tailored geometries. By carefully designing the surface contour of the interchangeable end effector, the hybrid soft robot could selectively lift low surface energy objects.

2. Materials and methods

2.1. Materials

The chemical components and self-healing mechanism of the 3D-printable, self-healing, adhesive elastomers investigated in this paper are shown in Fig. 1. Acrylic monomers 2-hydroxyethyl acrylate (HEA) (TCI) and butyl acrylate (BA) (Sigma-Aldrich) were used as the base material components. The photoinitiator (phenylbis(2,4,6-trimethylbenzoyl) phosphineoxide) (BAPO) and dithiol 2,2-(ethylenedioxy)diethanethiol (EDDT) were purchased from Sigma-Aldrich. Thiol–Michael-based sulfone diacrylate (TMSDA) was synthesized according to previously documented procedures.[31] A commercially available green photoblocker was obtained from Kroger comprised of Fd&c Yellow #5, tartrazine (trisodium 5-hydroxy-1-(4-sulfonatophenyl)-4-[(*E*)-(4-sulfonatophenyl)-diazenyl]-1*H*-pyrazole-3-carboxylate),[32] and Fd&c Blue #1 Brilliant blue FCF (disodium;2-[[4-[ethyl-[(3-sulfonatophenyl)methyl]amino]phenyl]-[4-[ethyl-[(3-sulfonatophenyl)methyl]azaniumylidene]cyclohexa-2,5-dien-1-ylidene]methyl]benzenesulfonate).[33]

2.2. Mixing, casting, and 3D printing

Mixing. The photoinitiator was combined with BA, HEA, and TMSDA (Table 1) and mixed until fully dissolved in amber vials.

Casting. For tension specimens, mixed resins were cast into 5.1 mm deep poly(tetrafluoroethylene) (PTFE) molds. Each tensile specimen was 45.5 mm long with a 17 mm gauge length and 7 mm gauge width tapering up to an overall width of 14 mm over a 9 mm radius.[34] Photopolymerization was carried

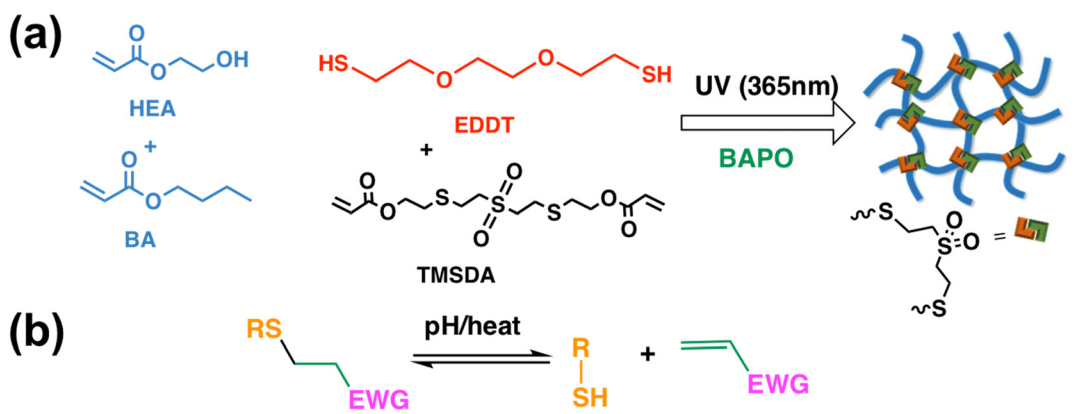

Fig. 1 (a) Photopolymerization of adhesive acrylate elastomer materials. (b) Reversible Thiol–Michael reaction.

Table 1 Compositions of the seven different formulations explored in this study

Formulation	HEA[a]	BA[a]	TMSDA[b]	EDDT[b]
1	50	50	1	0.75
2	50	50	1	1
3	67	33	1	0.75
4	80	20	1	0.75
5	80	20	1	1
6	100	0	1	0.75
7	100	0	1	1

[a] Listed as weight percentage of rubber fraction. [b] Listed as percent hard rubber (phr).

out by a broad spectrum UVA photoreactor of intensity 3.3 ± 0.2 mW cm^{-2} for 20 min as outlined in the literature.[35,36] Samples were then left to rest for 24 h. For lap shear specimens, mixed resins were cast, using a micropipette, into 25.4 mm by 25.4 mm silicone molds (Mold Max 29NV, Smooth-On) with an estimated depth of 1.68 mm. Photopolymerization was carried out by a broad spectrum UVA photoreactor of intensity 3.3 ± 0.2 mW cm^{-2} for 20 min as outlined in the literature.[35,36] Samples were then left to rest for 24 h.

3D printing. A modular digital light processing (DLP) 3D printing system (Figure 4 Standalone, 3D Systems) was used for 3D printing. A commercially available green photoblocker was used to ensure dimensional fidelity. Actuator prints were produced 20° from the horizontal build orientation, while the University of Miami logo and Eiffel tower were produced flat to the build plate. All prints used a layer thickness of 100 μm and standard manufacturer-recommended settings for the other process parameters. Cure depth, which indirectly controls light intensity and exposure time through a proprietary algorithm in the Figure 4 DLP printer, was set to 300 μm. Finished parts were removed from the build plate, immersed in 99% pure isopropyl alcohol (Fisher Scientific) to dissolve any liquid resin, and sonicated in an ultrasonic cleaner (VWR 750, Global Industrial) for 5 min. Parts were then left to air dry for a minimum of 30 min (robot actuators >3 h), then post-cured in a UV light box (LC-3D Print Box, NextDent) for 5 min.

2.3. Mechanical testing

2.3.1. Tension testing. Quasi-static uniaxial tension testing was conducted under ambient conditions on an Instron 3344 universal testing machine. The machine was equipped with a 100-N load cell for force measurement and a built-in crosshead displacement measurement. Thin, flat, dumbbell-shaped specimens (see Section 2.2) were mounted using screw side-action tensile grips. All tests were conducted at a constant crosshead speed of 50 mm min^{-1}. The dimensions of the gage section and overall length of each undeformed specimen were measured using digital calipers. Engineering (tensile) stress was calculated as force divided by undeformed gage cross-sectional area, and engineering (tensile) strain as crosshead displacement divided by undeformed overall length. Three specimens were tested for each formulation.

2.3.2. Lap shear testing. Quasi-static lap shear (simple shear) testing was conducted under ambient conditions on an Instron 3365 universal testing machine following methods similar to ASTM D1002. The machine was equipped with a 2 kN load cell for force measurement and a built-in LVDT sensor for crosshead displacement measurement. 115 mm long by 25.4 mm wide by 3.175 mm thick rectangular laps were machined to size from (303 stainless steel, 6061 aluminum, poly(tetrafluoroethylene) (PTFE), polystyrene, polypropylene, and polyoxymethylene) sheet stock (McMaster-Carr) or 3D printed from a 1.75 mm PLA spool (Prusament PLA) using a desktop 3D printer (Original Prusa i3 MK3S, Prusa Research). Prior to binding, the laps were cleaned using laboratory wipes (Kimwipes, Kimberly-Clark) and 99% pure isopropyl alcohol (Fisher Scientific). Square test specimens (nominally 25.4 mm in-plane and 1.68 mm thick; see Section 2.2) were bound to the laps directly from the mold. A 500 g cylindrical weight was placed on the lap binding area for 60 s to ensure consistent binding pressure. After the weight was removed, the lap-specimen setup was allowed to rest for 5 min prior to testing to allow the specimen to elastically relax post-binding. The lap-specimen setup was mounted in the universal testing machine using pneumatic side-action grips. 3D-printed horizontal spacers were inserted between the grips and the laps to ensure alignment of the specimen, laps, and load train. Engineering (shear) stress was calculated as force divided by original lap-specimen binding area. Differences between nominal specimen dimensions and as-built dimensions were quantified and deemed to be statistically insignificant. Thus, the original binding area of 25.4 mm by 25.4 mm was taken to be the nominal planar area of the test specimen. Note that this shear stress is the average shear stress on the planar faces of the specimen, not the local shear stress that varies pointwise within the faces. Engineering (shear) strain was calculated as the crosshead displacement divided by the nominal thickness of the adhesive specimen (*i.e.*, 1.68 mm). A minimum of three specimens per formulation or lap type were tested.

3. Results and discussion

3.1. Material formulation

HEA and BA monomers were chosen to make the acrylic polymer backbone of the designed adhesive elastomer materials (Fig. 1(a)). The hydrogen bonding afforded by the hydroxyl groups of HEA can contribute to adhesion, while a soft, tacky character is typically imbued through the incorporation of BA. The inclusion of dithiol molecules (EDDT), which act as chain transfer agents during free radical polymerization of acrylates, serves to widen the molecular weight distribution in the system. It provides low molecular weight oligomers *via* early termination to a thiol, but also high molecular weight polymers when propagation proceeds on both sides of the dithiol molecule.[24] The low molecular weight components facilitate energy dissipation *via* plasticization, while the high molecular weight components provide load-bearing capacity in the polymer network. A small amount of crosslinking is also needed for these materials to exhibit elastic behavior, which is provided through the dynamic diacrylate crosslinker TMSDA. This molecule exploits reversible

Thiol–Michael chemistry (Fig. 1(b)) to provide bond reconfigurability at polymer network crosslinks. Based on prior work, ratios of EDDT and TMSDA were kept at TMSDA : EDDT = 1 : 0.75 or 1 : 1 (Table 1), since higher ratios of EDDT led to creep susceptibility, while lower ratios of EDDT inhibited dynamic exchange and self-healing.[24]

Variations in these molecules (Table 1) are explored to reveal their relative effect on mechanical and adhesive properties. In all cases, the native materials (without photoblocking additives) are clear and pale yellow and almost colorless.

3.2. Tensile testing results

Pristine specimens. Uniaxial tension testing was conducted to investigate the impact of composition on tensile properties (*e.g.*, ultimate tensile strength, elongation at break). Formulations 2 and 5 (Table 1) were prepared by changing the HEA : BA ratio (in wt%) from 50 : 50 to 80 : 20, respectively, while keeping the TMSDA : EDDT ratio (in phr) at 1 : 1. Engineering stress–strain curves obtained from uniaxial tension tests of formulations 2 and 5 are shown in Fig. 2(a) (black and red curves, respectively). Decreasing the amount of BA in the material system fundamentally altered the stress–strain profile (*e.g.*, higher early tensile modulus, more strain stiffening, and ultimately behavior consistent with plastic deformation before fracture), leading to significantly higher ultimate tensile strength and elongation at break. Specifically, materials with HEA : BA (80 : 20) demonstrated good ultimate tensile strength (> 200 kPa) and excellent elongation at break (> 2000%). As such, an 80 : 20 ratio of HEA : BA was used as a baseline for further variations in composition.

The ratio of TMSDA : EDDT, in percent hard rubber (phr), was changed from 1 : 1 to 1 : 0.75 (Table 1, formulation 5 to 4) to investigate the effect of EDDT on tensile properties. The materials with less EDDT (1 : 0.75) exhibited stiffer stress–strain profiles, a narrower compliant region, and substantially less plastic-like deformation, culminating in similar ultimate tensile strengths but significantly lower elongations at break (Fig. 2(a), red and blue curves). Control samples without BA were prepared for both systems while keeping the TMSDA : EDDT ratios at 1 : 0.75 and 1 : 1 (Table 1, formulations 6 and 7). The control samples for TMSDA : EDDT (1 : 1) exhibited meaningfully higher ultimate tensile strengths than their BA-containing counterparts (Fig. S4, ESI†), but were observed to be substantially less tacky. Less significant differences in the stress–strain response were observed between control samples of TMSDA : EDDT (1 : 0.75) and the BA-incorporated samples (Fig. S2, ESI†).

Self-healed specimens. Dynamic properties of the TMSDA crosslinker after polymerization were confirmed using self-healing experiments on formulations 4 through 7. Pristine samples were cut orthogonal to their longitudinal axis (Fig. 2(b)) using a sharp blade. Both healed and uncut (control) samples were heated at 90 °C for 24 h before testing to activate self-healing through reorganization of dynamic thiol–Michael linkers. These self-healing conditions (90 °C for 24 h) were chosen based on literature data to ensure there is sufficient thermal stimulus to exchange thiol–Michael linkages,[24,37] but also enough time to allow equilibration of the crosslinks in the material.[31,38,39]

Notably, this heat treatment altered mechanical properties, perhaps by increasing polymer conversion or by the loss of plasticizing species (*cf.* Fig. 2(a) and (b)). Materials with formulation 5 exhibited > 95% recovery of stress and ~ 87% recovery of strain as shown in Fig. 2(b). Similarly, self-healing data from formulation 7 controls demonstrated ~ 100% recovery of the tensile stress and strain (Fig. S1, ESI†). Self-healing experiments on formulation 4 and formulation 6 with lower EDDT content, displayed in Fig. 2(b) and Fig. S3 (ESI†), showed reduced self-healing efficiency. Formulation 4 gave 50% recovery of stress and ~ 80% recovery of strain, and formulation 6 showed ~ 25% stress recovery and 30% strain recovery (Fig. S3, ESI†). The superior self-healing with higher EDDT content is expected, as EDDT helps generate shorter chains in the network that improve polymer diffusion and hence facilitate healing. Comparing the self-healing of formulation 5 (Fig. S6 and S7, ESI†) with HEA : BA = 80 : 20 to formulation 7 (Fig. S14 and S15, ESI†) with

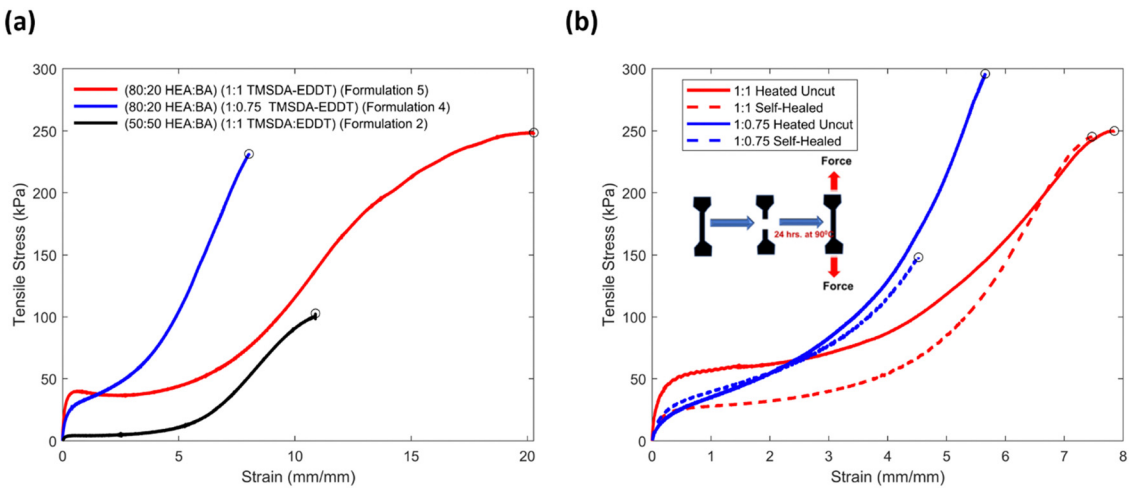

Fig. 2 Engineering stress–strain curves obtained from uniaxial tension testing of (a) pristine materials with different ratios of HEA : BA and TMSDA : EDDT, and (b) self-healed materials with HEA : BA (80 : 20) and two different TMSDA : EDDT ratios, 1 : 1 and 1 : 0.75.

HEA : BA = 100 : 0, both having TMSDA : EDDT = 1 : 1 phr, both show essentially complete self-healing. This suggests that the shorter, more mobile chains generated with higher EDDT content is more significant for self-healing efficiency than the HEA content.

3.3. Lap shear testing results

Lap shear (simple shear) tests were performed in three phases to investigate the adhesive properties of various formulations, substrate materials, and adhesion conditions. The first set of tests compared the shear stress at failure of different adhesive formulations bonded to PLA laps at room temperature. In the second phase of testing, a single adhesive (formulation 4) was tested on a variety of lap (substrate) materials. In the third and final phase of testing, the impact of heated binding (90 °C for 16 hours) on specimen-lap adhesion was evaluated.

The adhesive properties of the different material formulations in Table 1 were explored as shown in Fig. 3(a) using printed poly(lactic acid) (PLA) laps. Fig. 3(a) shows both the average, standard deviation, and best-measured shear stress at failure for each formulation. With TMSDA : EDDT (1 : 0.75), as HEA content increases from HEA : BA (50 : 50) to (100 : 0) (formulations 1, 3, 4, 6), there is a general trend of increasing shear strength (Fig. 3(a)). The mean of formulation 6 (HEA : BA = 100 : 0), however, was slightly lower than that of formulation 4 (HEA : BA = 80 : 20). These lap shear tests tended to fail adhesively (Table S1, ESI†), indicating the cohesive (internal shear) strength of the material exceeded the adhesive (lap-material adhesion) strength.

The superior performance of formulation 4, which contains 80% HEA and 20% BA, and formulation 6, which contains 100% HEA, with both having 0.75 phr EDDT, is likely due to several factors. Higher BA content reduces tensile modulus and strength (Fig. 2(a)). Formulation 4 with 20% BA represents a material with higher tackiness (Fig. 3(a)), and thereby better adhesion to the substrate, without substantial loss of mechanical strength. Additionally, formulation 5 had a higher content of EDDT than formulation 4 (1 phr *vs.* 0.75), which can induce more plastic-like deformation (Fig. 2(a)), reducing the cohesive strength of the material, leading to internal failure prior to debonding from the laps (Table S1, ESI†).

Overall, materials with a small fraction of BA (20%) adhere better to PLA than those with higher BA content. Additionally, BA (20%) gives slightly improved adhesion to PLA when compared to materials with no BA. Higher EDDT content appears to adversely impact material cohesive strength, leading to cohesive failure at 1 phr EDDT. This suggests that there is a tradeoff between the adhesive characteristics to PLA, which increases with HEA content and reaches a peak near 80% BA, and material cohesive strength, which decreases with EDDT content.

The adhesive strength of formulation 4 against a variety of substrates (laps) is shown in Fig. 3(b). These substrate materials included 303 stainless steel, 6061 aluminum, poly(tetrafluoroethylene) (PTFE), 3D-printed PLA, polystyrene, polypropylene, and polyoxymethylene. Aluminum showed the highest average shear stress at failure, outside of PLA, perhaps due to the higher concentration of metal oxide species on the surface able to participate in hydrogen bonding. Steel had a lower average shear stress at failure, and had a significantly lower variability than aluminum. The tests with aluminum laps exhibited more variability, likely due to inconsistent surface roughness between laps.

The polymeric substrates (PTFE, polystyrene, polypropylene and polyoxymethylene), however, generally exhibited lower shear strengths than the aluminum substrate and typically resulted in adhesive failure (*i.e.*, interfacial adhesion strength was lower than the material's internal shear strength). PLA exhibited notably higher shear strengths, likely due to lap surface roughness from 3D printing enhancing interfacial adhesion. Polypropylene and polyoxymethylene exhibited higher "best values" than the other plastics, but with high variability. It is important to note that good adhesion was observed across the full range of substrates, including low surface energy materials such as PTFE and polyoxymethylene that are typically challenging to adhere to.

Steel was selected as the material for heated binding tests due to its low variability. Materials that were bonded at elevated temperature had ~7 fold better adhesive properties compared to materials that were bonded at room temperature (displayed

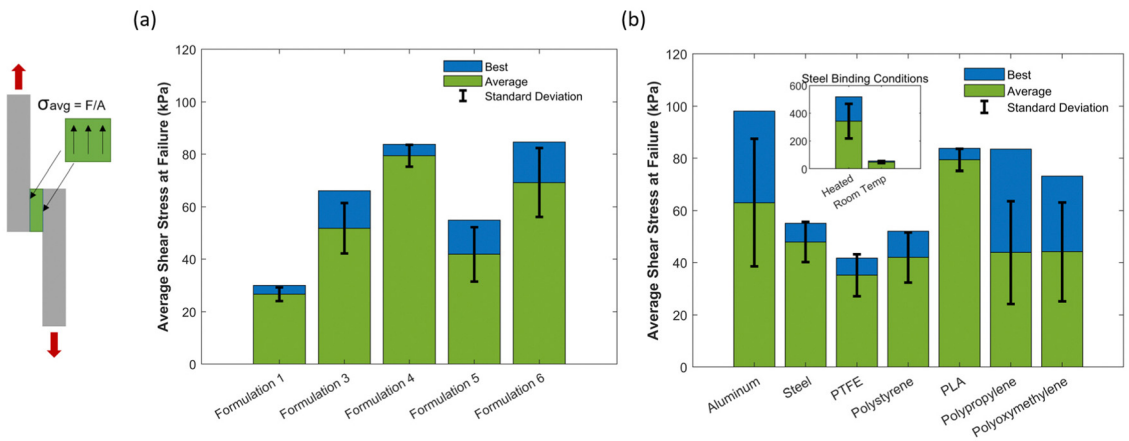

Fig. 3 Average shear stress at failure from lap shear testing (a) for different formulations on PLA laps and (b) of formulation 4 (TMSDA : EDDT (1 : 0.75) with HEA : BA (80 : 20)) on different laps.

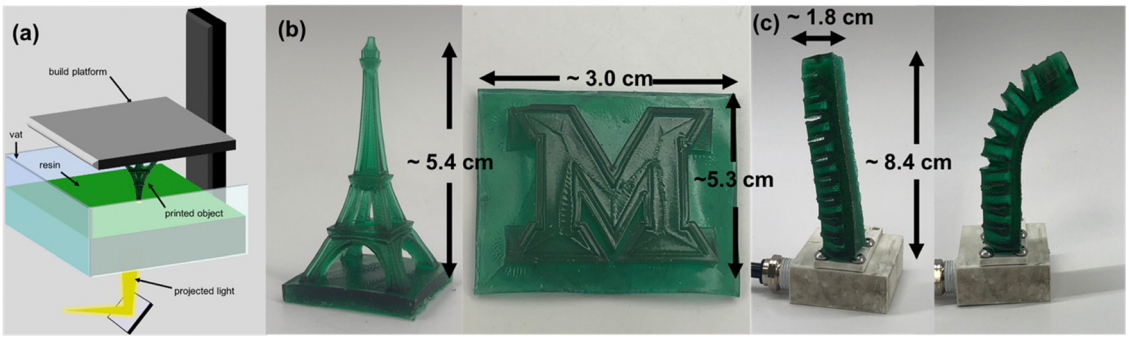

Fig. 4 (a) Schematic of the DLP 3D-printing process used to produce (b) the Eiffel tower, Miami University logo, and (c) a one-piece pneumatic actuator. All prints utilized formulation 4 with HEA : BA (80 : 20) and TMSDA : EDDT (1 : 0.75).

in the inset of Fig. 3(b)). All tests after heating resulted in cohesive failure, indicating that the adhesion strength of the steel–elastomer interface exceeded the internal shear strength of the material. This is likely due to (a) the increased modulus of the elastomer after heat treatment and (b) reconfiguration of the dynamic covalent bonds in the TMSDA at 90 °C, enabling a new permanent shape that occupies irregularities in surface topology, thereby leading to superior mechanical coupling and adhesion (Fig. S17, ESI†). This improvement in adhesion is a valuable characteristic for an adhesive elastomer as bonding can be reversible at room temperature to facilitate applications, but permanent and strong with applied heat and pressure.

3.4. Printability and functionality demonstrations

The DLP 3D printability (Fig. 4(a)) of the adhesive elastomers was evaluated and optimized to produce relevant test structures using formulation 4 as a representative base material. As illustrated in Fig. 4(b), the complex Eiffel tower and Miami University logo were successfully printed with high resolution. In addition, a one-piece pneumatic actuator was printed to investigate the functionality of prints with internal voids (Fig. 4(c)). The actuator was capable of pneumatic inflation, leading to meaningful movement and actuation.

The adhesive functionality of prints was demonstrated through reconfigurable stick-on "fingertips," printed with formulation 4,

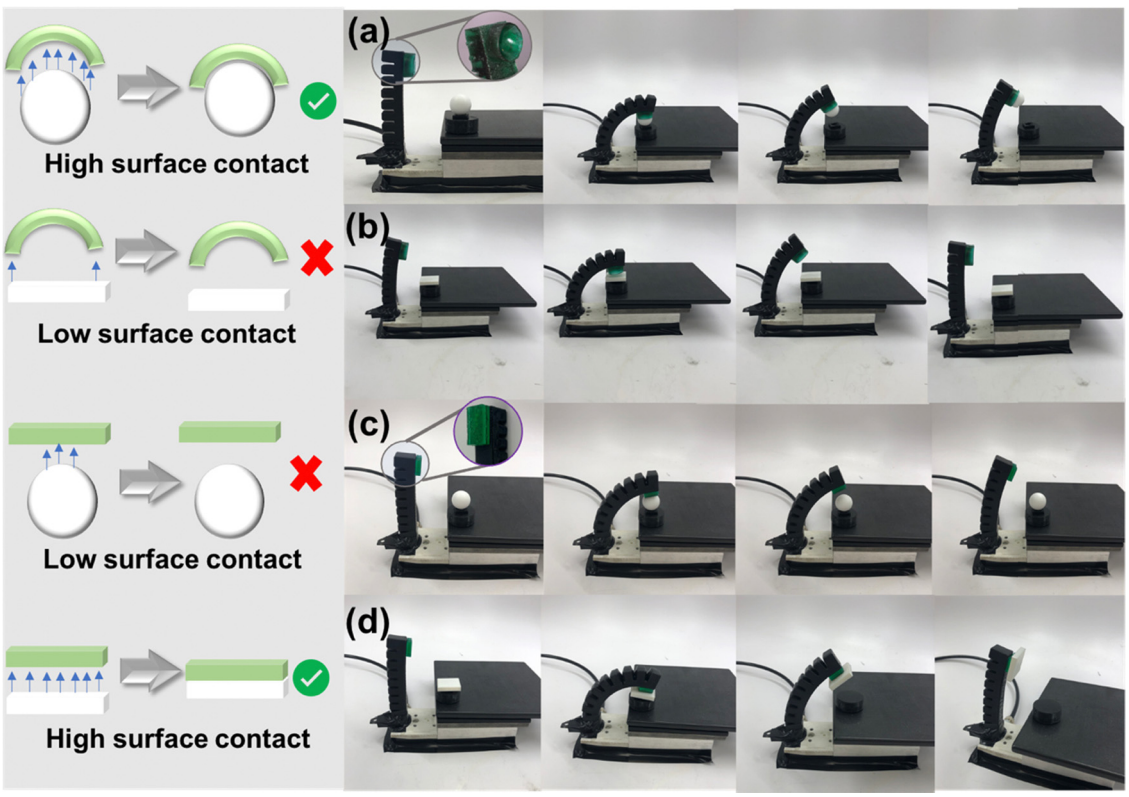

Fig. 5 Demonstrations of the functionalized actuator (a) successfully lifting a PTFE ball using a concave adhesive "fingertip," (b) failing to lift a rectangular PLA block using a concave adhesive "fingertip," (c) failing to lift a PTFE ball using a flat adhesive "fingertip," and (d) successfully lifting a rectangular PLA block using a flat adhesive "fingertip".

which could selectively lift objects (Fig. 5). A pneumatic actuator printed using the commercial elastomeric resin RUBBER-65A BLK (3D Systems) was developed as a scaffold for shape-selective adhesion. On its own, the actuator had no adhesive properties or the ability to pick up objects. To increase the functionality of the actuator, shape-selective 3D-printed adhesive "fingertips" were adhesively bound to the end of the actuator. These interchangeable end effector "fingertips" were either flat or concave surfaces that could selectively attach to flat or round objects, respectively. The adhesive "fingertips" were either rectangular (2.5 × 2.5 × 0.49 cm) or concave (cylinder of diameter 2.2 cm, height of 0.89 cm, with the concave shape achieved within a spherical geometry of diameter 1.9 cm).

As shown in Fig. 5, selectivity could be achieved using the adhesive "fingertip" modified RUBBER-65A BLK actuator to lift a sphere (PTFE, 8 g, 1.9 cm diameter) or rectangular block (3D-printed PLA, 3 g, 1.9 × 1.9 × 0.64 cm). Different substrate materials were chosen to highlight shape selectivity across different surface energies. When the shape of the adhesive fingertip and the object were compatible with sufficient interfacial contact, the object was successfully lifted by the actuator (Movies 1 and 2, ESI†; Fig. 5(a) and (d)). When the shape of the fingertip and object were incompatible with insufficient interfacial contact, the actuator failed to lift the object (Movies 3 and 4, ESI†; Fig. 5(b) and (c)). In this way, simple functionalization of a generic pneumatic actuator towards shape selectivity can be achieved with easily 3D-printable resins. It is also noteworthy that the functionalized actuator can lift low surface energy materials such as a PTFE sphere or a moderate surface energy PLA block with high selectivity. It is important to note that various debonding mechanisms could be used to release the object. In this case, shear was applied to debond the lifted objects, but careful design of the actuator could be performed in future iterations to have a secondary actuation that changes the contact area, thereby debonding objects. Additionally, in this paper, the curvature of the adhesive finger was carefully matched to the curvature of the object to be lifted. However, it is also possible to design partial mismatch of curvature if selective debonding is targeted.

4. Conclusions

In this work, elastomeric materials with both adhesive and self-healing properties were prepared using UV-initiated photopolymerization. Self-healing properties were incorporated *via* thermoresponsive dynamic Thiol–Michael chemistry. These materials exhibited excellent self-healing properties (~100% efficiency) and strong adhesion to a range of metallic and polymeric surfaces. Additionally, heating during binding improved the adhesive properties significantly, resulting in higher average shear stress at cohesive failure compared to materials bonded at room temperature. The 3D printability of these materials was demonstrated on a commercial DLP system by printing objects with complex geometric features such as internal voids. Additionally, the adhesive materials were shown to add functionality to existing soft robotic actuators through shape-selective lifting of low surface energy materials, making them attractive candidates for sorting applications.

Author contributions

S. W. and B. J. contributed to the data curation, investigation, methodology, formal analysis, and writing (original draft; review and editing). R. R. and G. E. contributed to the investigation, methodology, and formal analysis. A. C. contributed to the conceptualization, investigation, methodology, and supervision. J. B. contributed to the methodology and writing (review and editing). T. O. contributed to the conceptualization and supervision. C. T., R. L., and D. K. contributed to the conceptualization, methodology, supervision, and writing (review and editing).

Conflicts of interest

The authors declare no conflicts.

Acknowledgements

R. R. was supported by the University of Dayton SURE Program. The Konkolewicz group gratefully acknowledges support from the National Science Foundation under grant no. (DMR-1749730) for dynamic materials synthesis and tensile testing. The full research team thanks Braeden Windham and Nathan Maleski of the University of Dayton Research Institute for machining the laps used during simple shear testing.

References

1 F. Awaja, M. Gilbert, G. Kelly, B. Fox and P. J. Pigram, *Prog. Polym. Sci.*, 2009, **34**, 948–968.
2 M. Tang, Z. Li, K. Wang, Y. Jiang, M. Tian, Y. Qin, Y. Gong, Z. Li and L. Wu, *J. Mater. Chem. A*, 2022, **10**, 1750–1759.
3 H. Wang, M. Totaro and L. Beccai, *Adv. Sci.*, 2018, **5**, 1800541.
4 L. F. M. da Silva, A. Öchsner and R. D. Adams, *Handbook of adhesion technology*, Springer, 2011, vol. 1.
5 L. F. M. Da Silva and M. J. C. Q. Lopes, *Int. J. Adhes. Adhes.*, 2009, **29**, 509–514.
6 Z. Xu, L. Chen, L. Lu, R. Du, W. Ma, Y. Cai, X. An, H. Wu, Q. Luo and Q. Xu, *Adv. Funct. Mater.*, 2021, **31**, 2006432.
7 X. Ji, M. Ahmed, L. Long, N. M. Khashab, F. Huang and J. L. Sessler, *Chem. Soc. Rev.*, 2019, **48**, 2682–2697.
8 G. Grundmeier and M. Stratmann, *Annu. Rev. Mater. Res.*, 2005, **35**, 571.
9 H. J. Meredith and J. J. Wilker, *Adv. Funct. Mater.*, 2015, **25**, 5057–5065.
10 C. R. Matos-Perez, J. D. White and J. J. Wilker, *J. Am. Chem. Soc.*, 2012, **134**, 9498–9505.
11 E. M. Petrie, *Handbook of adhesives and sealants*, McGraw-Hill Education, 2007.
12 J. Chen, Y. Shi, J. Yang, N. Zhang, T. Huang and Y. Wang, *Polymer*, 2013, **54**, 464–471.

13 K. Li, X. Zan, C. Tang, Z. Liu, J. Fan, G. Qin, J. Yang, W. Cui, L. Zhu and Q. Chen, *Adv. Sci.*, 2022, **9**, 2105742.
14 J. Rao, Y. Zhou and M. Fan, *Polymers*, 2018, **10**, 266.
15 S. Wang and M. W. Urban, *Nat. Rev. Mater.*, 2020, **5**, 562–583.
16 S. V. Wanasinghe, E. M. Schreiber, A. M. Thompson, J. L. Sparks and D. Konkolewicz, *Polym. Chem.*, 2021, **12**, 1975–1982.
17 J. Tang, L. Wan, Y. Zhou, H. Pan and F. Huang, *J. Mater. Chem. A*, 2017, **5**, 21169–21177.
18 T. Jing, X. Heng, X. Guifeng, C. Ling, L. Pingyun and G. Xiaode, *Polym. Chem.*, 2021, **12**, 4532–4545.
19 S. Dai, M. Li, H. Yan, H. Zhu, H. Hu, Y. Zhang, G. Cheng, N. Yuan and J. Ding, *Langmuir*, 2021, **37**, 13696–13702.
20 Z. Zhang, N. Ghezawi, B. Li, S. Ge, S. Zhao, T. Saito, D. Hun and P. Cao, *Adv. Funct. Mater.*, 2021, **31**, 2006298.
21 C. Lou, E. Liu, T. Cheng, J. Li, H. Song, G. Fan, L. Huang, B. Dong and X. Liu, *ACS Omega*, 2022, **7**, 5825–5835.
22 K. Lei, M. Chen, X. Wang, J. Gao, J. Zhang, G. Li, J. Bao, Z. Li and J. Li, *J. Mater. Chem. B*, 2022, **10**, 9188–9201.
23 J. Z. Gul, M. Sajid, M. M. Rehman, G. U. Siddiqui, I. Shah, K.-H. Kim, J.-W. Lee and K. H. Choi, *Sci. Technol. Adv. Mater.*, 2018, **19**, 243–262.
24 E. F. Gomez, S. V. Wanasinghe, A. E. Flynn, O. J. Dodo, J. L. Sparks, L. A. Baldwin, C. E. Tabor, M. F. Durstock, D. Konkolewicz and C. J. Thrasher, *ACS Appl. Mater. Interfaces*, 2021, **13**, 28870–28877.
25 A. U. H. Meem, K. Rudolph, A. Cox, A. Andwan, T. Osborn and R. Lowe, in International Manufacturing Science and Engineering Conference, American Society of Mechanical Engineers, 2021, vol. 85079, p. V002T06A031.
26 C. J. Thrasher, J. J. Schwartz and A. J. Boydston, *ACS Appl. Mater. Interfaces*, 2017, **9**, 39708–39716.
27 C. Fu, Z. Xia, C. Hurren, A. Nilghaz and X. Wang, *Biosens. Bioelectron.*, 2022, **196**, 113690.
28 T. J. Wallin, J. Pikul and R. F. Shepherd, *Nat. Rev. Mater.*, 2018, **3**, 84–100.
29 D. Rus and M. T. Tolley, *Nature*, 2015, **521**, 467–475.
30 E. Roels, S. Terryn, F. Iida, A. W. Bosman, S. Norvez, F. Clemens, G. Van Assche, B. Vanderborght and J. Brancart, *Adv. Mater.*, 2022, **34**, 2104798.
31 P. Chakma, S. V. Wanasinghe, C. N. Morley, S. C. Francesconi, K. Saito, J. L. Sparks and D. Konkolewicz, *Macromol. Rapid Commun.*, 2021, 2100070.
32 National Center for Biotechnology Information, PubChem Compound Summary for CID 164825, Tartrazine, **https://pubchem.ncbi.nlm.nih.gov/compound/Tartrazine**, (accessed 23 May 2023).
33 National Center for Biotechnology Information, PubChem Compound Summary for CID 19700, Brilliant Blue FCF., **https://pubchem.ncbi.nlm.nih.gov/compound/Brilliant-Blue-FCF**, (accessed 23 May 2023).
34 A. R. Kemper, A. C. Santago, J. D. Stitzel, J. L. Sparks and S. M. Duma, *J. Biomech.*, 2012, **45**, 348–355.
35 K. A. Miller, O. J. Dodo, G. P. Devkota, V. C. Kirinda, K. G. E. Bradford, J. L. Sparks, C. S. Hartley and D. Konkolewicz, *Chem. Commun.*, 2022, **58**, 5590–5593.
36 J. C. Dowdy and R. M. Sayre, *Photochem. Photobiol.*, 2013, **89**, 961–967.
37 B. Zhang, P. Chakma, M. P. Shulman, J. Ke, Z. A. Digby and D. Konkolewicz, *Org. Biomol. Chem.*, 2018, **16**, 2725–2734.
38 B. Zhang, Z. A. Digby, J. A. Flum, P. Chakma, J. M. Saul, J. L. Sparks and D. Konkolewicz, *Macromolecules*, 2016, **49**, 6871–6878.
39 P. Chakma, Z. A. Digby, J. Via, M. P. Shulman, J. L. Sparks and D. Konkolewicz, *Polym. Chem.*, 2018, **9**, 4744–4756.